SANDIA REPORT

SAND2005-7208
Unlimited Release
Printed November 2005

Adaptive Optical Zoom Sensor

Brett E. Bagwell, William C. Sweatt, David V. Wick

Prepared by
Sandia National Laboratories
Albuquerque, New Mexico 87185 and Livermore, California 94550

Sandia is a multiprogram laboratory operated by Sandia Corporation,
a Lockheed Martin Company, for the United States Department of Energy's
National Nuclear Security Administration under Contract DE-AC04-94AL85000.

Issued by Sandia National Laboratories, operated for the United States Department of Energy by Sandia Corporation.

Available to DOE and DOE contractors from
U.S. Department of Energy
Office of Scientific and Technical Information
P.O. Box 62
Oak Ridge, TN 37831

Telephone: (865)576-8401
Facsimile: (865)576-5728
E-Mail: reports@adonis.osti.gov
Online ordering: http://www.osti.gov/bridge

Available to the public from
U.S. Department of Commerce
National Technical Information Service
5285 Port Royal Rd
Springfield, VA 22161

Telephone: (800)553-6847
Facsimile: (703)605-6900
E-Mail: orders@ntis.fedworld.gov
Online order: http://www.ntis.gov/help/ordermethods.asp?loc=7-4-0#online

SAND2005-7208
Unlimited Release
Printed November 2005

Adaptive Optical Zoom Sensor

David V. Wick and Brett E. Bagwell
Intelligent Perception
Department 06646

William C. Sweatt
Applied Photonic Microsystems
Department 017131

Sandia National Laboratories
P.O. Box 5800
Albuquerque, NM 87185-0570

Abstract

In order to optically vary the magnification of an imaging system, continuous mechanical zoom lenses require multiple optical elements and use fine mechanical motion to precisely adjust the separations between individual or groups of lenses.[1] By incorporating active elements into the optical design, we have designed and demonstrated imaging systems that are capable of variable optical magnification with no macroscopic moving parts.[2-3] Changing the effective focal length and magnification of an imaging system can be accomplished by adeptly positioning two or more active optics in the optical design and appropriately adjusting the optical power of those elements. In this application, the active optics (e.g. liquid crystal spatial light modulators or deformable mirrors) serve as variable focal-length lenses.[4-7] Unfortunately, the range over which currently available devices can operate (i.e. their dynamic range) is relatively small. Therefore, the key to this concept is to create large changes in the effective focal length of the system with very small changes in the focal lengths of individual elements by leveraging the optical power of conventional optical elements surrounding the active optics. By appropriately designing the optical system, these variable focal-length lenses can provide the flexibility necessary to change the overall system focal length, and therefore magnification, that is normally accomplished with mechanical motion in conventional zoom lenses.

Keywords: Active optics, Adaptive optics, Deformable Mirrors, MEMS, Spatial light modulators, Liquid crystals, Zoom systems

This page intentionally left blank

Contents

Figures

Tables

1. Introduction

Speed, size, weight and power requirements have limited or completely prohibited the use of mechanical zoom lenses in many applications. A zoom lens is simply an optical system that can vary magnification or focal length while keeping the image plane stationary. Conventional technology requires a continuous zoom lens to have multiple optical elements and uses coupled motion to adjust the axial separations between individual or groups of elements in order to vary the optical magnification.[1] Mechanical zoom lenses such as those found on 35 mm cameras may take hundreds of milliseconds to vary magnification and are restricted to magnifying the area on-axis (i.e. the system must be directly pointed at the area to be magnified). Discrete, multiple field-of-view (FOV) systems have been developed that vary magnification by rotating lenses or groups of lenses in and out of the optical path. These are also limited to on-axis magnification. Digital or electronic zoom increases the size of the image, but without any increase in information content (i.e. resolution). With digital zoom, the individual pixels on the focal plane array are simply remapped to larger areas in the display, as in Figure 1(b), and thus it is extremely fast and is not limited to on-axis magnification. By changing the true magnification of the system, optical zoom increases the resolution over the magnified area-of-interest, Figure 1(c).

Gimbals, which are used to redirect the instantaneous FOV of an imaging system, often weigh as much as the entire optical system. Depending on the size of the optics and the speed of the gimbal, they can draw hundreds or even thousands of Watts to slew large-aperture systems. Even with state-of-the-art gimbals, they take hundreds of milliseconds to slew large angles and may induce unwanted jitter or require momentum compensation.

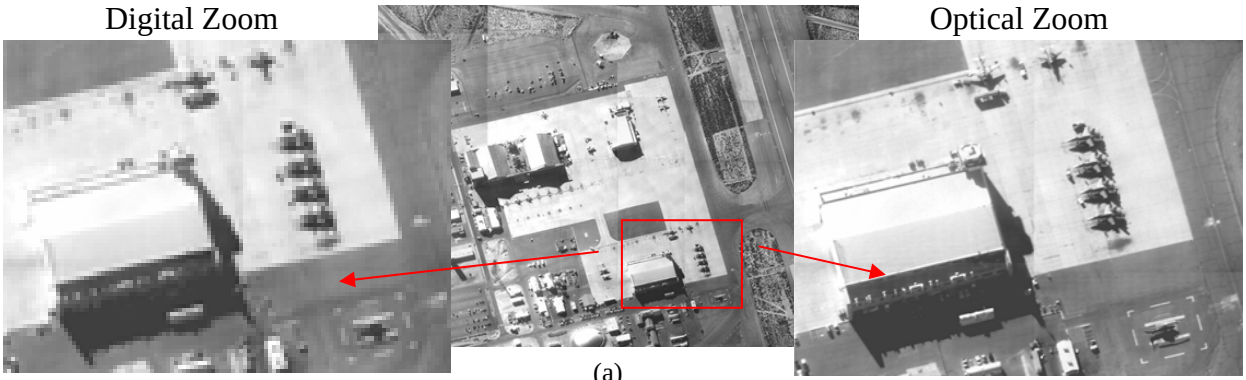

Figure 1. Overhead image of an airfield (a), magnified by 3.8X (b) electronically (digitally), and (c) optically.

In order to achieve true optical magnification and overcome deficiencies in size, weight, and power requirements, we have previously proposed a revolutionary alternative to conventional mechanical zoom systems where moving lenses/mirrors and gimbals are replaced with active optics.[2-3] Active or adaptive optics,[8] such as liquid crystal (LC) spatial light modulators (SLMs) and deformable mirrors (DMs), have previously been proposed and demonstrated as variable focal-length elements.[5-7] Focus control is accomplished by systematically adjusting the optical path across the element to add/subtract quadratically varying phase. In fact, any aberration can be added or subtracted (focus is simply a low order aberration), providing a tremendous amount of flexibility.[9-11] By applying the appropriate voltage to each pixel or actuator, the optical path

can be adjusted to create an optical wavefront that approximates the wavefront produced by a conventional lens or mirror. By changing those voltages appropriately, the "focal length" of the active element can be varied within the limits set by the dynamic range and the number of pixels or actuators. More recently, liquid lenses, which use an "electrowetting effect", have been used as variable focal-length lenses for on-axis magnification.[12] While these lenses appear to perform satisfactorily for low-cost applications such as cell phone cameras, the wavefront quality is not (yet) sufficient for high-resolution applications.

Through judicious optical designs, these variable focal-length elements can provide the flexibility necessary to change the overall system focal length, and therefore magnification, that is normally accomplished with mechanical motion. The key to this concept is to create relatively large changes in system magnification with very small changes in the focal lengths of individual elements by leveraging the optical power of conventional optical elements surrounding the active optics. In addition to changing the focal length with a DM or SLM, optical tilt can also be added to the wavefront by appropriately adjusting the voltages. This allows magnification of ***any*** point within the FOV without physically moving some portion of the optical system. Thus, the object to be magnified does not have to lie on the optical axis as in a conventional system.

Using liquid crystal SLMs, we previously designed and demonstrated this concept in the laboratory.[2-3] Although currently available, transmissive LC SLMs lack the phase retardance and number of pixels necessary to adequately change the focal length of the individual element, we were able to create a quasi-Fresnel zone plate that mimics the behavior of a lens.[13] The drawback to using the SLMs in this fashion is the overall efficiency, since only a portion of the light is diffracted into the correct converging wavefront. Potentially an even bigger problem is that a significant portion of the improperly focused light still makes it to the image plane and adds unwanted noise, masking the image of interest. For most real-world applications, using the SLMs as diffractive zone plates in this manner is unacceptable; however, this preliminary experiment served to prove the viability of the concept and demonstrate the basic principles that were applied to this effort. Figure 2 shows the image of an AF resolution bar chart taken with our liquid crystal SLM, active optical zoom system. In (a), the system is set to image a wide FOV with the bar chart located in the upper right quadrant. When we changed the voltages applied to the two SLMs in the optical train, applying both defocus and tilt, we achieved 3.3X magnification, with a corresponding increase in resolution capability, as shown in (b). By introducing optical tilt to the SLMs (simply by changing the voltage scheme that is applied), any area within the FOV can be magnified, and that area can be changed on a millisecond time scale.

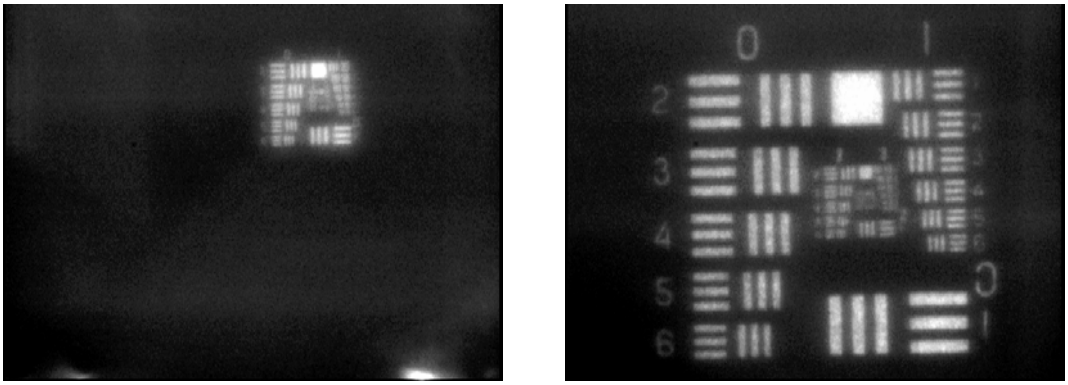

(a) (b)

Figure 2. AF resolution bar chart using a 3.3X SLM-based, active optical zoom sensor.

2. Reflective Adaptive Optical Zoom Sensor

It should be noted that much of the work contained in Section 2 started in FY04 from other funding sources. While we have highlighted the significant accomplishments that were achieved exclusively as part of this LDRD, we have included some of those earlier results as relevant introductory/background material.

2.1 Designing the Optical Zoom System

Focus control of DMs is accomplished in a fashion similar to that used with the LC SLMs. The reflective surface can be adjusted to produce a wavefront that is approximately the same as one produced by a conventional curved mirror, and the focal length of the DM can be varied within the limits set by the maximum deflection (i.e. dynamic range) and the number of actuators. The key to achieving high quality imaging with an active optical zoom system is to precisely control the applied voltages, and thus the mirror surface, of the DMs to create pure defocus while minimizing other aberrations. Thus, at any given instant, the DM will act just as a diffraction-limited static mirror, but it will have the ability to change focal-length by simply changing the applied voltages. In theory, we should also be able to add the correct amounts of tilt and higher order aberrations, along with defocus, to magnify any area within the wide FOV.

In order to demonstrate the concept with an all-reflective system, we utilized small, electrostatically-driven micromachined deformable membrane mirrors (MDMMs) from OKO Technologies along with conventional spherical mirrors in our optical design. Custom software was developed by Narrascape to simultaneously control both MDMMs in the optical setup. Each individual actuator or any group of actuators on either mirror can be controlled via a graphical user interface, Figure 3. To further manage the values of the MDMMs, independent control of the first fourteen Zernike polynomials (not including Piston) was integrated. Two other features, Solo and Mute, were added to allow us to quickly remove and add individual Zernike contributions independently.

Designing an optical system with significant magnification around the limited capabilities of these mirrors was our next technical hurdle. As with the LC SLMs, deformable mirrors, both MDMMs and conventional, can operate over very limited focal-length ranges, and creating large changes in system magnification with small changes in the focal lengths of individual components proved to be a difficult task. However, by leveraging those small changes in focal length with high optical-power static elements, we were able to successfully design an all-reflective, active optical zoom sensor with 4X magnification, shown in Figure 4(a). While our ZEMAX® design was optimized for only two positions, zoomed and unzoomed, we found that by adding an iterative slider, the far right “Zoom Control” in Figure 3, we were able to move continuously between the wide FOV and the narrow FOV with decent imaging throughout. However, there remained a significant amount of residual aberration in our system, and our early attempts to manually remove this residual aberration were not very successful.

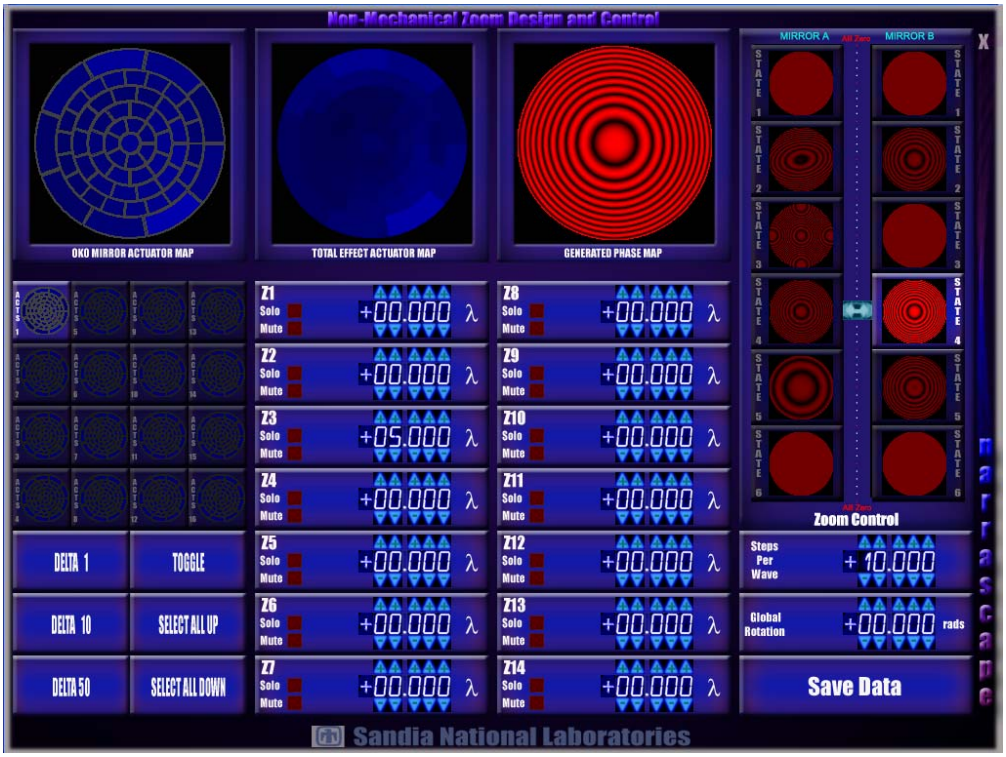

Figure 3. User control interface for two MDMMs with individual actuator and Zernike control applied (Z3 is defocus). The slider on the far right allows us to move iteratively between states.

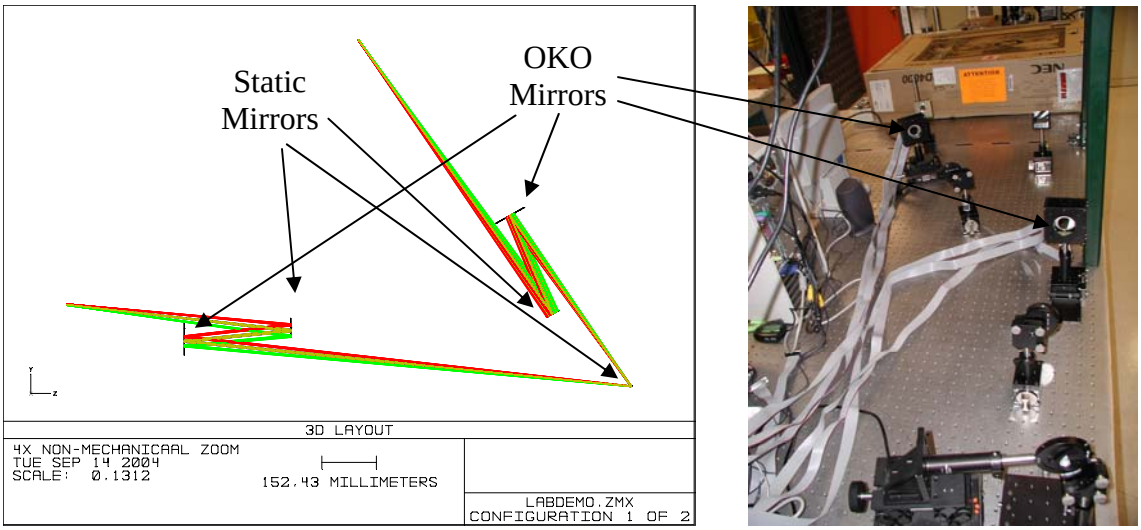

(a) (b)

Figure 4. (a) ZEMAX® and (b) experimental layouts of the 4X active optical zoom.

2.2 Calibrating the Micromachined Deformable Membrane Mirrors

High-resolution imaging applications that utilize micromachined deformable membrane mirrors (MDMMs) require precise wavefront control. In order to obtain high-fidelity images, exact wavefront control must be achieved without introducing significant amounts of unwanted aberrations.[14,15] As part of our development in active optical zoom, we evaluated the wavefront control from both a 37-channel and two 59-channel MDMMs from OKO Technologies. Our

goal was to adjust the applied voltage scheme in order to produce the required defocus while reducing any residual aberrations below the diffraction-limited threshold.

Characterization of the mirrors was done using a Michelson interferometer with a static, spherical mirror of known focal-length positioned in the reference leg and an MDMM in the test leg, see Figure 5. Using a custom Shack-Hartmann wavefront sensor, each leg is measured independently. First, a frame grabber records the positions of the focused spots on the CCD with the static mirror to use as a reference. Those positions are shown graphically in the top-left corner above 'Wavefront Sensor' of Figure 6. Next, with the static mirror blocked, an adaptive optics (AO) control algorithm developed by Narrascape is used to drive the MDMM in order to match the test wavefront to the reference wavefront.

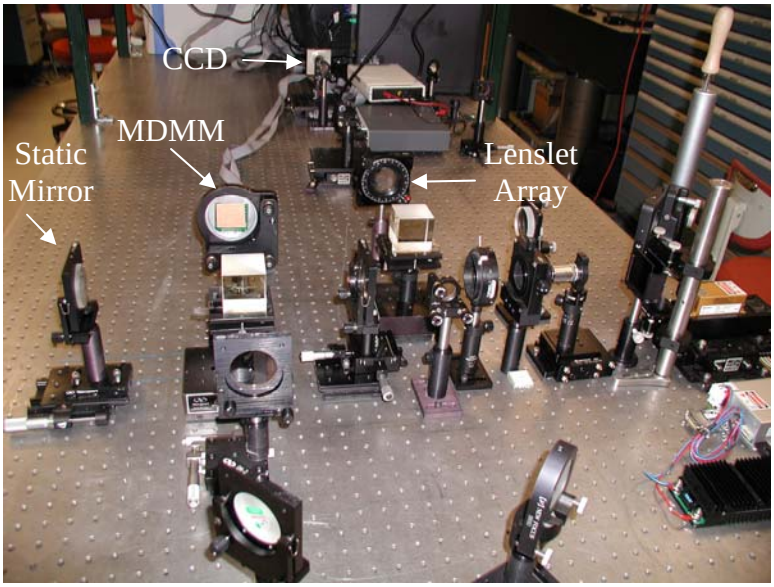

Figure 5. Adaptive optics testbed with the 37-Channel MDMM mirror.

Using a static mirror with a radius of curvature of 5m (f = 2.5m) in the reference leg, the average residual error of the entire system was measured to be less than 0.25 waves (P-V) at 532nm, although there was a significant dynamic contribution due to 1) thermals in the air and 2) vibrations on the table. With the static mirror covered, the control algorithm was able to drive the 37-channel OKO MDMM in the test leg to a stable solution. A color-coded representation of the control voltages that were applied in order to correct the 37-channel OKO MDMM are shown above 'Mirror Maximum' in Figure 6. Notwithstanding the dynamic fluctuations, the residual error was nominally diffraction limited over the central ~80% of the aperture. Because the MDMMs are mounted around the edge of the reflective surface, it is impossible to fully correct the wavefront over the entire aperture. Residual aberrations near the edge of the mirrors should be considered in system design.

When both the reference and MDMM wavefronts propagate through the system, we observe interference fringes, as expected. An interferogram, generated from the f = 2.5m reference mirror and the unbiased, "flat" MDMM, is shown in Figure 7. Here the bull's-eye pattern simply shows the defocus that must be applied to the MDMM in order to match the curvature of the static mirror. There is clearly some residual aberration at the edge of these mirrors that causes the fringes to blur, and this will affect imaging capability.

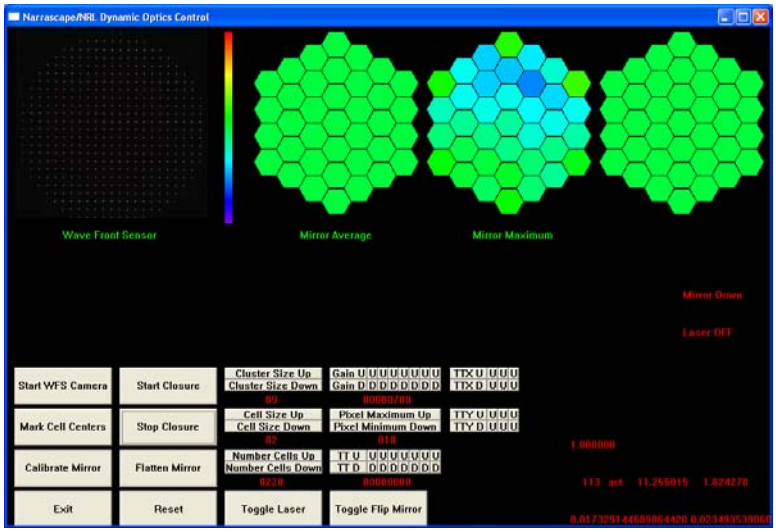

Figure 6. Adaptive optics closed-loop control interface for 37-Channel MDMM.

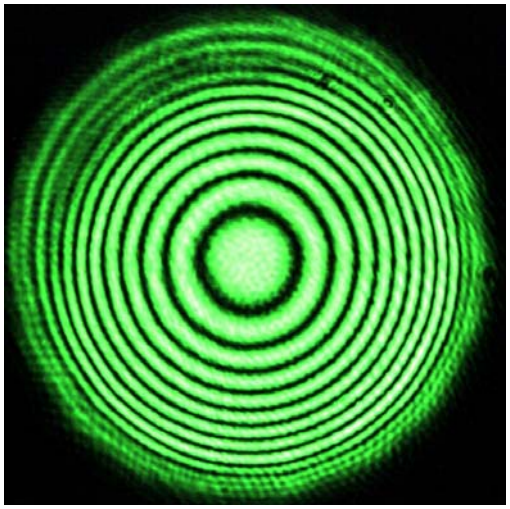

Figure 7. Interferogram from the unbiased, "flat"37-channel OKO MDMM and a diffraction-limited static mirror with focal length f = 2.5m in a Michelson interferometer.

In order to match the mirror figure of the MDMM to that of the static mirror, the AO control algorithm starts with a prescribed bias voltage that is applied to every actuator on the mirror. That bias voltage was predetermined through a simple, manual focus test (power through a pinhole at the desired focus spot). Figure 8(a) shows an interferogram when the biased mirror is compared to the static reference mirror. In contrast to Figure 7, there are only a few waves of optical path difference. As the adaptive optics loop attempts to reach a diffraction-limited solution, most of the residual error is eliminated, as seen in 8(b). The wavefront is near diffraction-limited over the central ~80% of the MDMM.

By modifying the control algorithm, we were also able to apply the AO loop to two 59-channel MDMMs. One of the mirrors was capable of matching the curvature of an f = 5m mirror, while the other was limited to f = 7.5m. (We did not have a static mirror with a focal length between f = 5m and f = 7.5m for testing.) The before and after correction images of the f = 7.5m mirror are shown below in Figure 9. As was the case with the 39-channel mirror, the boundary conditions

at the edge prohibit correction over the whole aperture, but the central ~70% of the mirror is near diffraction limited after the AO control algorithm reaches a stable solution.

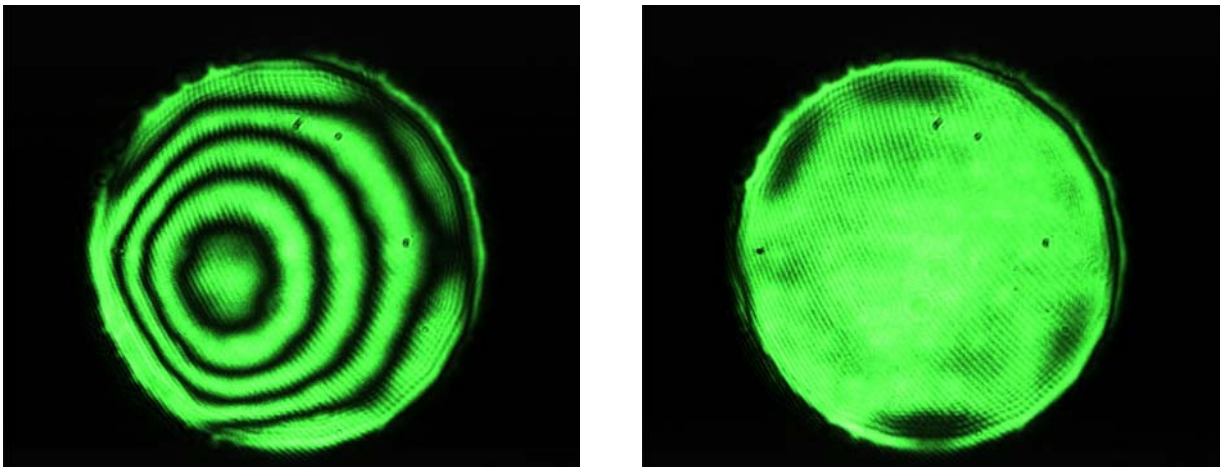

(a) (b)

Figure 8. Interferogram from (a) a biased 37-channel OKO MDMM and a static mirror with focal length f = 2.5m in a Michelson interferometer. As the closed-loop algorithm approaches a solution in (b), the residual fringes have nearly disappeared.

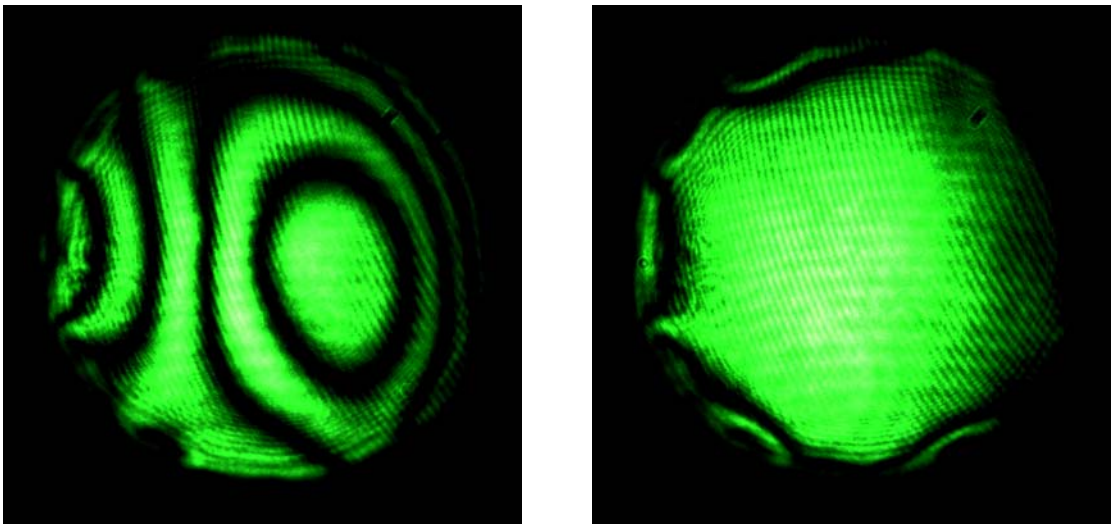

(a) (b)

Figure 9. Interferogram from (a) a biased 59-channel OKO MDMM and a static mirror with focal length f = 7.5m in a Michelson interferometer. As the closed-loop software approaches a solution in (b), the residual fringes have nearly disappeared.

2.3 Experimental Results

Figure 4 shows the ZEMAX® and experimental layout of the active optical zoom demonstration. This system consists of two 59-channel OKO MDMMs and 3 static spherical mirrors with focal lengths of 1.0m, -0.2m, and 1.0 m. The calculated magnification for this system is 4X with a corresponding increase in resolution of approximately 2X. The resulting images, shown in Figure 10, show an increase in magnification of about 3.8X. Here Groups 2-5 of an AF bar chart

are imaged on the camera. Compare the image quality when the MDMMs are replaced with static, diffraction-limited spherical mirrors in Figure 11. Note that the camera gain is manually adjusted between (a) and (b) for each of the figures.

(a) (b)

Figure 10. (a) Unzoomed and (b) zoomed images taken with active optical zoom system. Nothing was changed between (a) and (b) except the voltages that were applied to the actuators and the gain on the camera.

(a) (b)

Figure 11. (a) Unzoomed and (b) zoomed images taken with same system using static, diffraction-limited spherical mirrors. Note that in this case, the static mirrors were changed between (a) and (b) in order to achieve "zoom".

The difference in resolution between the horizontal bars and vertical bars is due to the off-axis design, and likely some slight misalignment; because of the off-axis design, the tolerances are extremely tight in the x-z plane (i.e. the plane of the optical bench). Nonetheless, we are very pleased that the quality of the active optical zoom images are comparable to the static case. We are also excited by the fact that we can move quasi-continuously between the zoomed and unzoomed states. Note that the poor quality at the edges of the images, particularly noticeable in corners of Figure 10(a), is due to the residual errors at the edge of the MDMMs. Because these

mirrors are attached at this boundary, it is very difficult to remove all of the aberrations at the edges. Ideally, we would aperture the mirror down and only use the central ~80% of the mirrored surface.

If we restrict the FOV of our system, we can eliminate some of the edge effects. Figures 12 and 13 show another set of images taken with slightly increased magnification using both active and static zoom, respectively. Again, the systems perform nearly identically in terms of resolution capability. Here the unzoomed images, Figures 12(a) and 13(a), are digitally expanded 4X in order to compare resolution with the zoomed images. In this case, the changes in image brightness/color are simply due to manual adjustments of the camera gain.

In both figures, there is nearly two times the resolution capability in the zoomed case, consistent with MTF calculations. The highest resolvable set of horizontal bars in the unzoomed image from the active optical zoom system, 12(a), is Group 4-2 at 17.95 lp/mm (as measured in the object plane). We achieved slightly better resolution with the static mirrors in Figure 13(a), where Group 4-3 at 20.16 lp/mm is resolvable. These are consistent with the calculated cut-off frequency of 23 lp/mm and an MTF that falls below 10% at 20 lp/mm. In the zoomed case, we can resolve Group 5-1 at 32 lp/mm in both the active optical zoom system and the static system (although that is not necessarily clear in Figure 12(b)). This is again consistent with a calculated cut-off frequency of 43 lp/mm and an MTF that falls below 10% at 36 lp/mm.

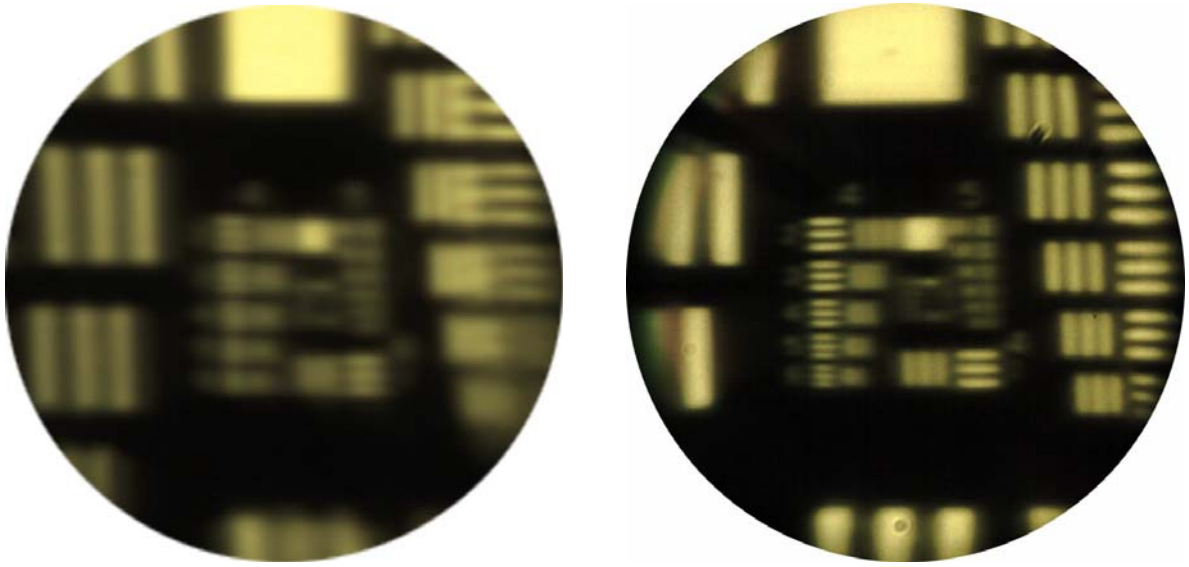

(a) (b)

Figure 12. Restricted FOV images taken with active optical zoom system in (a) unzoomed (electronically expanded by 4X) and (b) zoomed configurations. Note the increase in resolution capability.

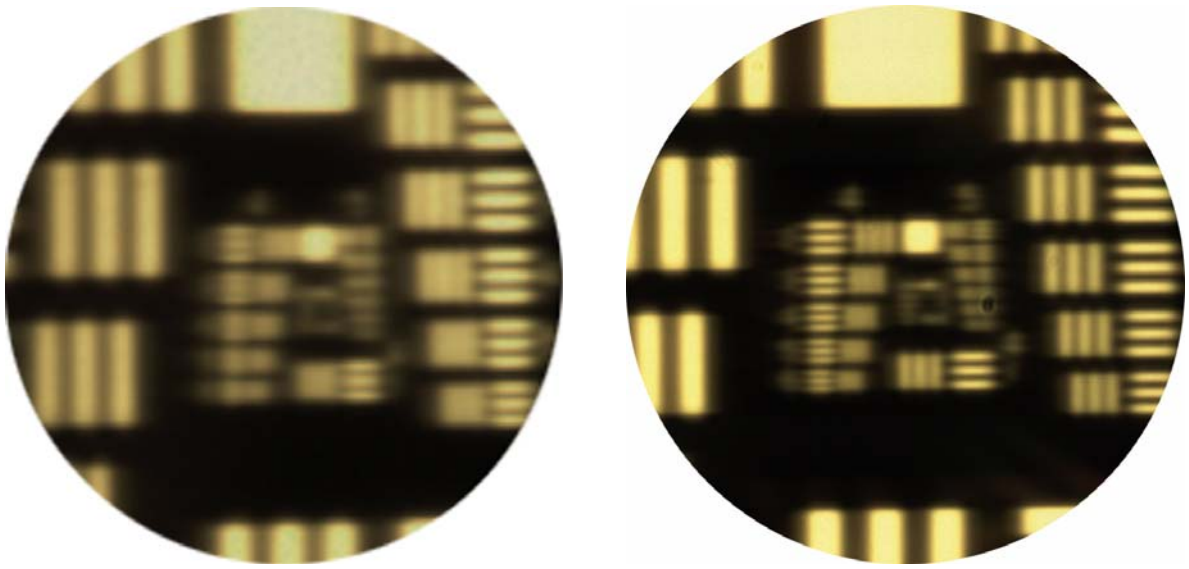

(a) (b)

Figure 13. Restricted FOV images taken with static, diffraction-limited spherical mirrors in the system in (a) unzoomed (electronically expanded by 4X) and (b) zoomed configurations. Again, the static mirrors had to be physically changed between (a) and (b) in order to accomplish the "zoom" that the active optical system achieved through adjusting the applied voltage scheme. Note that changes in intensity/color are simply due to manual adjustments of the camera gain.

3. Transmissive Adaptive Optical Zoom Sensor

Figure 2 showed the results of a previously assembled system using two liquid crystal (LC) spatial light modulators (SLMs) as Fresnel zone plates. Unfortunately, the optical efficiency from zone plates is limited, and the uncorrected light will mask the corrected image, essentially reducing the signal-to-noise ratio. As part of this LDRD, we investigated liquid crystal lenses for this application.

3.1 Liquid Crystal Lenses

Interest in using LC lenses has increased significantly due to the large birefringence and low voltage control. LC lenses are currently being developed as variable focal length elements.[16, 17] There are several structures that have been used or proposed for addressing LC lenses, but in all cases, the focal length of the lens is changed by simply changing the voltage that is applied to the lens or switching the polarization of the incoming light. Some of the potential applications for these lenses include optical interconnects, optical tweezers, machine vision, cell phone cameras, and tunable eye glasses. While sufficient for demonstrating basic capability, currently available lenses have limited clear apertures (< 6 mm) and dynamic ranges (infinity > f > 50 mm), and they do not have the high wavefront fidelity necessary for many military applications.

3.2 System Results

For our experiments, both commercially available LC lenses from OKO Technologies, and prototype LC lenses from Holochip, Inc. were used in a nonmechanical zoom demonstration. Each of these had limited dynamic range and aperture, which limited the f/# of our system to 55 (110 in the unzoomed case). Note that we chose to allow the f/# of our system to vary, which is actually a current topic of interest. By varying the f/#, we believe we can get larger changes in magnification, but the irradiance on the focal plane changes. We also loose resolution capability in the unzoomed case, which may or may not be acceptable.

Zoomed and unzoomed images of our system with about a 2X magnification using the OKO lenses are shown below in Figure 14. Because of the dispersive nature of these lenses, we limited the illumination to monochromatic light. Chromatic aberrations, therefore, will limit the useable bandpass of an active optical zoom system that utilizes these lenses. However, it is possible to sequentially cycle through multiple wavelengths. This concept is discussed in more detail in Section 4.

The improvement when we switched to the Holochip devices was dramatic. Figure 15 shows images taken with the same optical setup as Figure 14, only using the Holochip devices in place of the OKO lenses. The optical quality of the Holochip lenses was significantly better. However, the switching time for the Holochip lenses was on the order of 20 seconds. Obviously this is too slow for most applications. We are currently working with Holochip to improve both the time response and the dynamic range of their devices.

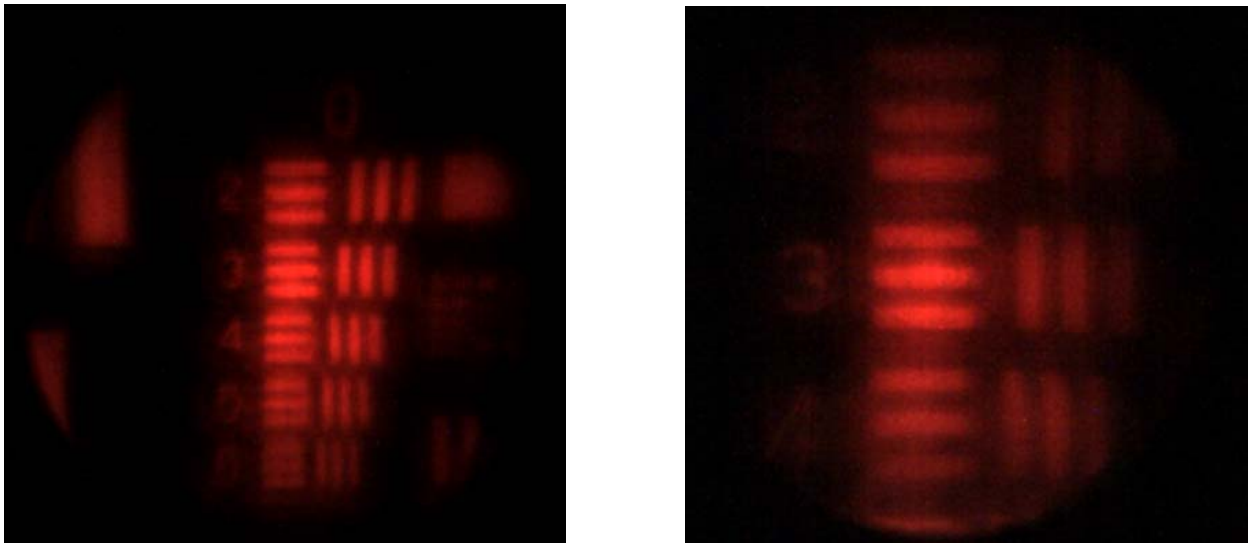

Figure 14. Images from transmissive nonmechanical zoom system using commercially available, liquid crystal lenses from OKO Technologies.

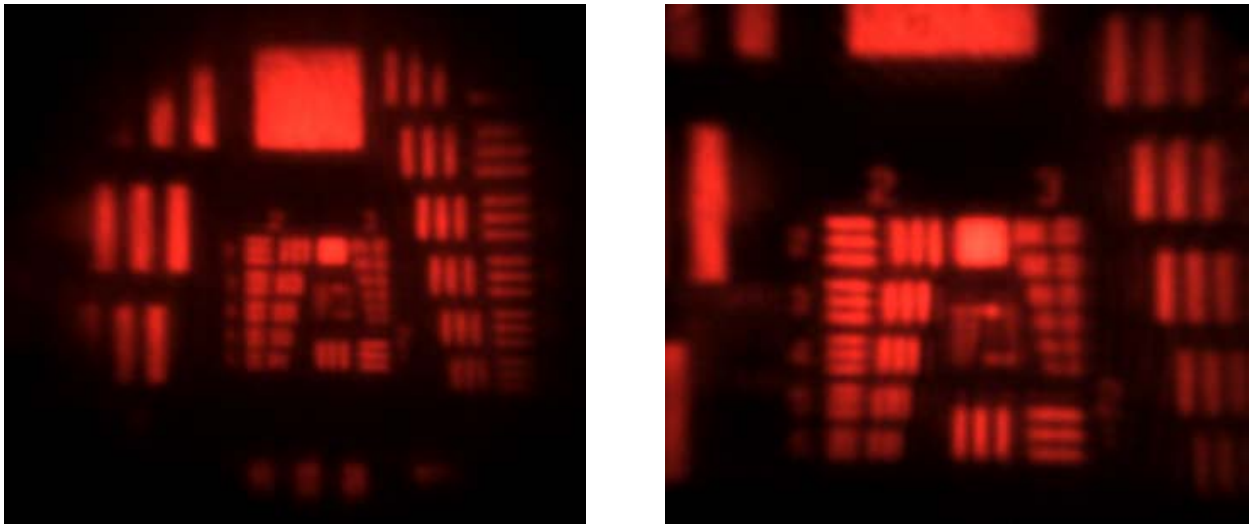

Figure 15. Images from transmissive nonmechanical zoom system using prototype liquid crystal lenses from Holochip, Inc.

4. Multi-spectral Compensation

4.1 Background

As we began investigating the LC lenses, we found that the dispersion in the devices limited the useable optical bandwidth. SLMs, which were also considered for this application, utilize 2π resets in order to create a Fresnel lens. 2π resets are only exact at one wavelength, so these are even more severely limited in bandwidth. As part of this LDRD, Brett Bagwell devised a concept for cycling through multiple wavelengths in rapid succession, and compensating the longitudinal chromatic aberrations with the LC lens itself.

The basic idea is to include a nonmechanical bandpass filter in the system. As longitudinal chromatic aberration is simply a change in focal length for different wavelengths, the LC lenses themselves can be adjusted to compensate the change in focal distance. Thus, we have achieved a nonmechanical solution to multispectral, active optical zoom and other active imaging systems using LC devices. We have submitted a Technical Advance on this concept.

4.2 Active/Passive Polarization Interference Filter

Previous efforts at non-mechanical spectral filtering in an adaptive optical imaging system utilized acousto-optic tunable filters (AOTF).[18] Wavelength selectivity is accomplished via diffraction from a variable frequency acoustic standing wave. The advantages of such a device are tunability and narrow pass band. Typical disadvantages of AOTF's are large packaging size, small clear aperture, and small acceptance angles.

We chose to explore a commercially available (switchable) polarization interference filter, in conjunction with a custom passive filtering stage, available from ColorLink Inc. This allowed us to greatly reduce packaging constraints and increase the useable FOV. The clear aperture of this device is 35 mm, the total thickness (including both passive and active stages) is 15 mm, and it accepts F/2.2 or slower.

Both the passive and active stages of the polarization interference filter rely on retarder stack filters (RSF's) between a polarizer and analyzer, an extension of the concepts described by Lyot (1933) and improved on by Solc (1965). RSF's are fabricated from stretched polycarbonate layers, and selectively rotate the polarization state of one or more wavelengths. The number of layers, amount of retardation, and orientation of these films dictate the pass-band of an individual stage. The active filter adds liquid crystal layers to selectively or sequentially control the polarization state of each color channel.[19, 20] The main disadvantage of polarization interference filters is the loss of light (50%) from an un-polarized image. Since the LCSLMs already require polarized light, this was not a consideration.

4.3 Measured Performance

Unfortunately, this device arrived too late in the year to incorporate it into our zoom systems, although we do hope to integrate it in future demonstrations. However, we were able to measure the bandpass of the device, which is the key first step in the optical design process. The product of the individual (broad) pass band of the active stage, shown in Figure 16(a), with the notched passive stage, shown in (b), resulted in the measured transmission spectra shown in (c). The

center wavelengths and HWHM for each channel are: Red: 630 ± 13 nm. Green: 538 ± 9 nm. Blue: 475 ± 5 nm.

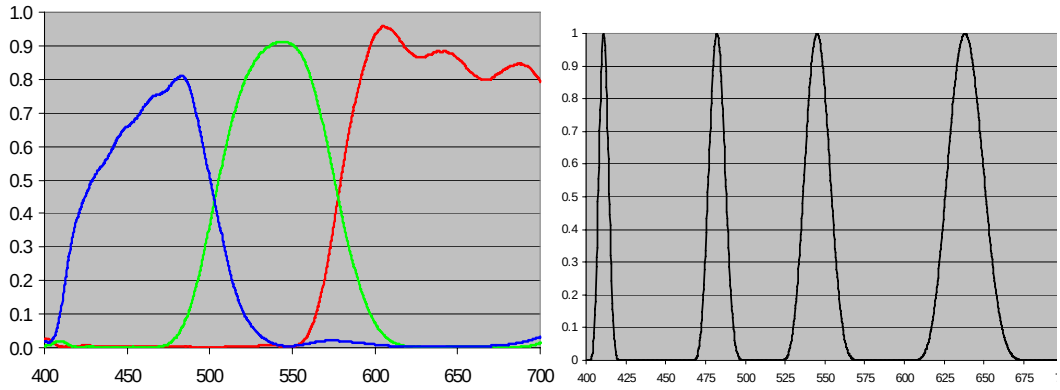

(a) (b)

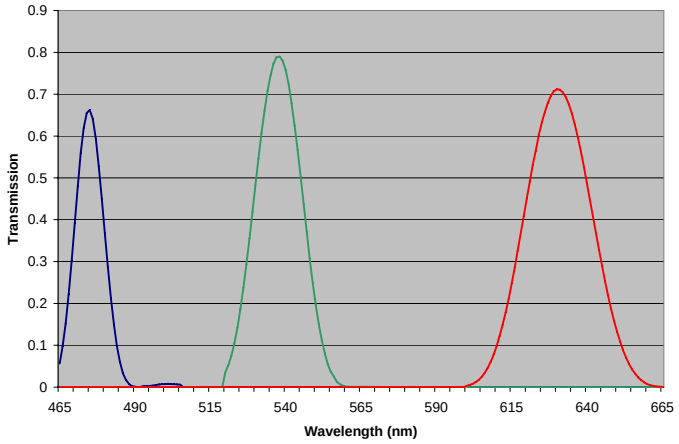

(c)

Figure 16. Polarization Interference Filter Transmission

As the switching speed of this device is on the order of a few tens of milliseconds, active polarization interference filters, when used in conjunction with wavelength dependent active optics, appear to be a viable means to achieve multi-spectral active optical zoom.

5. MEMS Requirements for Adaptive Optical Zoom

Segmented arrays of micromirrors offer a robust alternative to the continuous face sheet membrane mirrors described in Section 2 if some scattered light is tolerable. The arrays of micromirrors can be either square arrays of square mirrors or hexagonal arrays of hexagonal mirrors. Further, the micromirrors can have only piston motion, thus requiring only one actuator and drive signal per mirror, or they can have three motions, allowing piston motion and tilt motions in two dimensions. Here, the reduction in the wavefront errors (WFE) are computed for defocus, the third-order Zernike aberrations, and 5^{th} order spherical aberration as a function of the number of micromirrors in the array. [The other fifth-order aberrations have less RMS curvature and slope than does fifth-order spherical, so their residual aberration will be less.] These calculations will allow the effectiveness of the four mirror configurations to be compared.

For the adaptive optical zoom application, the optical system needs to be nearly diffraction limited. Therefore, the optical system's root-mean-square (RMS) wavefront error after optimal correction using the micromirror array is compared with the RMS WFE without the micromirror system. The mathematical expressions are first generated to describe the reduction in RMS WFE for a general wavefront aberration. Then these expressions are used to examine the effectiveness of the different micromirror array configurations to correct some of the low-order Zernike aberrations—tilt, focus, 3^{rd} order astigmatism and coma, and 3^{rd} and 5^{th} order spherical aberrations.

5.1 WFE reduction for square arrays of piston/tip/tilt micromirrors

In this section expressions will be developed that quantify the reduction in the WFE provided by a square array of tip/tilt/piston micromirrors. Each micromirror is assumed to locally null the piston and slope errors of the Zernike wavefront component. Regardless of which Zernike component is being corrected by the mirror array, the major WFE remaining within a single micromirror's footprint will be the local defocus and astigmatism. (This assumes there are a sufficient number of micromirrors in the array).

So here is the approach to calculating the residual WFE after the micromirror array has corrected as much of a Zernike WFE as it can: First, assume the micromirror has been tilted to match the slope at the center of a given micromirror and the average piston error within the micromirror's footprint has been compensated. This leaves the local curvature of the wavefront as the dominant remaining error. The wavefront curvature at the center of the micromirror is computed and squared, and then integrated over the aperture of the micromirror. This is done for all micromirrors in the array and the results are summed. The result is then divided by the area of the whole array and the square root is taken to give the RMS residual wavefront error.

In the next few paragraphs the quadratic approximation to the wavefront is calculated. Included are the focus error measured at "best focus" and the two saddle-shaped astigmatism terms defining "x-y" astigmatism and 45^0 astigmatism. The size of the square micromirror is defined to be 2η by 2η, and the center of a given micromirror is located at x=a and y=b.

The residual defocus error is actually defocus balanced by piston to minimize the RSS WFE. In the following expression, $W_{defocus}(a,b,x,y)$ is the wavefront error due to defocus of the

micromirror centered at (a,b), and $d^2W(a,b)/dx^2$ and $d^2W(a,b)/dy^2$ are the curvatures of the wavefront at (a,b) in the x and y directions:

$$W_{defocus}(a,b,x,y) = [(d^2W(a,b)/dx^2+d^2W(a,b)/dy^2)/4]*\{x^2+y^2-2/3*\eta^2\}. \qquad 5.1\text{-}1$$

The two astigmatism components are:

$$W_{astig}(a,b) = [\{d^2W(a,b)/dx^2 - d^2W(a,b)/dy^2 \}/4]*\{x^2 – y^2\} \qquad 5.1\text{-}2$$

and

$$W_{ast45}(a,b) = [d^2W(a,b)/(dxdy) /2]*\{2xy\}, \qquad 5.1\text{-}3$$

where $d^2W(a,b)/dxdy$ is the 45^0 curvature.

These terms (Eqns. 5.1-1, 2 & 3) are all orthogonal to one-another when integrated over the square surface of the micromirror. Thus the root-sum of squares (RSS) of the WFE can be written as

$$RSS_{total}(a,b) \approx RSS_{defocus}(a,b) + RSS_{astig}(a,b) + RSS_{ast45}(a,b) \qquad 5.1\text{-}4$$

where

$$RSS_{defocus}(a,b) = \iint_{-\eta,-\eta}^{\eta\eta} \{ [W_{defocus}(a,b)]^2 \} dxdy, \qquad 5.1\text{-}5a$$

$$RSS_{astig.}(a,b) = \iint_{-\eta,-\eta}^{\eta\eta} \{ [W_{astig}(a,b)]^2 \} dxdy, \qquad 5.1\text{-}5b$$

and

$$RSS_{ast45}(a,b) = \iint_{-\eta,-\eta}^{\eta\eta} \{ [[W_{ast45}(a,b)]^2 \} dxdy. \qquad 5.1\text{-}5c$$

As noted above, the cubic and other terms of higher order are assumed to be negligible for moderately large numbers of micromirrors in the array.

Equations 5.1-5a, 5.1-5b, and 5.1-5c can be integrated to give:

$$RSS_{defocus}(a,b) = 32/45\ \eta^6 *[(d^2W(a,b)/dx^2+d^2W(a,b)/dy^2)/4]^2 \qquad 5.1\text{-}6a$$

$$RSS_{astig.}(a,b) = 32/45\ \eta^6 *[(d^2W(a,b)/dx^2-d^2W(a,b)/dy^2)/4]^2 \qquad 5.1\text{-}6b$$

and

$$RSS_{ast45}(a,b) = 16/9\ \eta^6 *[(d^2W(a,b)/(dxdy))/2]^2 \qquad 5.1\text{-}6c$$

These are orthogonal components of the wavefront error for an individual micromirror. These RSS errors can now be summed for all of micromirrors in the aperture to determine the total RSS WFE. For example, for defocus,

$$RSS_{defocus}(aperture) = 32/45\ \eta^6 * \sum_{m,n=0}^{max}\sum[(d^2W(a_m,b_n)/dx^2+d^2W(a_m,b_n)/dy^2\ )/4]^2 \qquad 5.1\text{-}7$$

Remember that an integral can be approximated by a sum:

$$\int F(x)dx \approx [\ F(0) + F(\Delta) + F(2\Delta) + F(3\Delta) \ldots .\ ]/\Delta \qquad 5.1\text{-}8$$

Replacing the sum in the eqn. 5.1-7 with an equivalent integral (similar to eqn. 5.1-8) results in the residual wavefront aberration over the whole aperture.

$$RSS_{defocus}(aperture) = 32/45\ \eta^6 * \iint [(d^2W(x,y)/dx^2+d^2W(x,y)/dy^2\ )/4]^2\ dxdy\ /\ [4\eta^2] \qquad 5.1\text{-}9$$

So

$$RSS_{defocus\ sq} = 8/45\ \eta^4 * \iint [(d^2W(x,y)/dx^2+d^2W(x,y)/dy^2\ )/4]^2\ dxdy \qquad 5.1\text{-}10a$$

Likewise,

$$RSS_{astig\ sq} = 8/45\ \eta^4 * \iint [(d^2W(x,y)/dx^2-d^2W(x,y)/dy^2\ )/4]^2\ dxdy \qquad 5.1\text{-}10b$$

and

$$RSS_{ast45\ sq} = 4/9\ \eta^4 * \iint [(d^2W(x,y)/dxdy\ )/2]^2\ dxdy \qquad 5.1\text{-}10c$$

The total RSS aberration for the whole wavefront is just the sum,

$$RSS_{p\text{-}t\text{-}t\ sq.} \approx RSS_{defocus\ sq} + RSS_{astig\ sq} + RSS_{ast45}\ . \qquad 5.1\text{-}11$$

These equations are valid for calculating the RSS residual wavefront error after a square array of piston/tip/tilt mirrors has removed as much aberration from a wavefront as possible. This formulation is valid for any aperture shape and any arbitrary wavefront error where the curvature of the WFE does not vary significantly across any one individual micromirror. (As a rule of thumb, a wavefront would "vary significantly" if it introduced errors greater than $\lambda/10$ within the aperture of a single micromirror.)

5.2 WFE reduction for square arrays of piston-only micromirrors

Piston-only micromirrors do not remove the tilt error within the aperture of a single micromirror. Therefore, the residual error is equal to the defocus and astigmatism terms calculated in section 5.1 plus the tilt errors. The tilt error is asymmetric about the center of the micromirror so it is orthogonal to the defocus and astigmatism terms, which are all symmetric about the center of the

micromirror. Hence the RSS contribution of the tilt can be calculated separately and then added to the RSS error of the symmetric terms 5.1-10a, b, &c.

The RSS WFE for tilt in the *x* direction of a single micromirror is:

$$RSS_x(a,b) = \iint_{-\eta,-\eta}^{\eta,\eta} (dW(a,b)/dx * x)^2 \, dxdy$$

$$= 4/3*\eta^4 \, (dW(a,b)/dx)^2 \qquad 5.2\text{-}1$$

So the sum of the RSS WFE contributions from all of the micromirrors in the array can be written as

$$RSS_{tilt\ sq} = \eta^2 /3 \iint\{(dW(x,y)/dx)^2 + (dW(x,y)/dy)^2\}dxdy \qquad 5.2\text{-}2$$

Note that the tilt in the *y* direction has also been included. And, as in section 5.1, the integral is over the aperture of the whole array.

The total RSS error for a piston-only micromirror array is then

$$RSS_{piston\ sq} \approx RSS_{tilt\ sq} + RSS_{p\text{-}t\text{-}t\ sq}. \qquad 5.2\text{-}3$$

And therefore, the root-mean-square wavefront error is

$$RMS_{piston\text{-}only\text{-}sq} \approx [RSS_{tilt\ sq} + RSS_{p\text{-}t\text{-}t\ sq}]^{0.5} \qquad 5.2\text{-}4$$

5.3 WFE reduction for hexagonal arrays of micromirrors

The WFE residuals of hexagonal tip/tilt/piston mirrors have been developed as though the micromirrors were round with a radius of ε. This introduces small but negligible errors if the area of the circle is chosen to give the same area as the hexagon [$\varepsilon = \nu*(3/\pi)^{0.5}$, where 2ν is a diagonal of the hexagon]. Note that the following expressions are quite similar to those for square micromirrors—only the first coefficient in each expression changes.

$$RSS_{defocus\ hex} = 1/9\ \varepsilon^4 * \iint [(d^2W(x,y)/dx^2 + d^2W(x,y)/dy^2)/4]^2 \, dxdy \qquad 5.3\text{-}1$$

$$RSS_{astig\ hex} = 1/6\ \varepsilon^4 * \iint [(d^2W(x,y)/dx^2 - d^2W(x,y)/dy^2)/4]^2 \, dxdy \qquad 5.3\text{-}2$$

and

$$RSS_{ast45\ hex} = 1/6\ \varepsilon^4 * \iint [(d^2W(x,y)/dxdy)/2]^2 \, dxdy \qquad 5.3\text{-}3$$

The total RSS aberration for a wavefront corrected by a hexagonal array or tip/tilt/piston micromirrors is:

$$RSS_{p\text{-}t\text{-}t\ hex} \approx RSS_{defocus\ hex} + RSS_{astig\ hex} + RSS_{ast45\ hex}. \qquad 5.3\text{-}4$$

Now let us turn our attention to a hexagonal array of piston-only micromirrors. The contribution to the RSS wavefront error due to the tilting of the wavefront at each micromirror is:

$$RSS_{\text{tilt hex}} = \varepsilon^2/4 \iint\{(dW(a,b)/dx)^2 + (dW(a,b)/dy)^2\}dxdy \qquad 5.3\text{-}5$$

The total error for a hexagonal array of piston-only micromirrors is then

$$RSS_{\text{piston hex.}} \approx RSS_{\text{tilt hex}} + RSS_{\text{p-t-t hex}}. \qquad 5.3\text{-}6$$

5.4 Reduction of the RMS WFE for some low order Zernike aberrations

Optical systems suffering from low order Zernike aberrations are examined. If the wavefront is corrected as well as possible by an array of micromirrors, how much will the RMS WFE be reduced? This question will be answered for tilt errors, defocus, astigmatism, third-order coma and spherical, and fifth-order spherical aberration. Fifth-order spherical varies as $w(r) \propto r^6$, while other fifth-order aberrations vary as r^5, r^4, etc.—that is, lower powers of r. Thus, a calculation of the WFE reduction associated with 5th order spherical will bound the WFE reduction associated with other 5th order aberrations.

As an example, in Section 5.4.1 the reduction in the RMS WFE for an optical system suffering from coma will be calculated. A square array of "N" micromirrors will be assumed, so in the unit radius aperture, there will be N micromirrors where

$$N = \pi/(4\eta^2). \qquad 5.4\text{-}1$$

In section 5.4.2 the reduction of the RMS WFE for the other aberrations will be tabulated. Both square and hexagonal array geometries are considered.

5.4.1 Reduction in RMS WFE for a coma wavefront error using a square array of tip/tilt/piston micromirrors

The normalized Zernike coma term[8] (Z7) is tilt-compensated to minimize the RSS WFE:

$$Z7(x,y) = (8)^{0.5} * x*[3(x^2 + y^2) - 2] \qquad 5.4.1\text{-}1$$

The derivatives required for equations 5.1-10 are

$$d^2\{Z7(x,y)\}/dx^2 = (8)^{0.5}\ 18\ x \qquad 5.4.1\text{-}2a$$

$$d^2\{Z7(x,y)\}/dy^2 = (8)^{0.5}\ 6\ x \qquad 5.4.1\text{-}2b$$

$$d^2\{Z7(x,y)\}/dxdy = (8)^{0.5}\ 6\ y \qquad 5.4.1\text{-}2c$$

After these expressions are substituted into equations 2.1-10 and the results are integrated, the result is:

$RSS_{p\text{-}t\text{-}t\ sq}(Z7) \approx 24\pi\ \eta^4$. 5.4.1-3

By comparison, the RSS WFE of the coma aberration without the micromirror correction is:

$RSS(Z7) = \pi$,

so the reduction in RSS WFE is the ratio,

$RSS\ Ratio_{p\text{-}t\text{-}t}(Z7) \approx 24\ \eta^4$.

Using equation 5.4-1, one can write the reduction in the RSS WFE in terms of the number of micromirrors in the array:

$RMS\ Ratio_{p\text{-}t\text{-}t}\ (Z7) \approx 15 / N^2$. 5.4.1-4

5.4.2 Reduction in RMS WFE for coma using piston-only micromirrors

The derivatives required for equation 5.2-2 are

$d\{Z7(x,y)\}/dx = (8)^{0.5}\ 9x^2 - 2$ 5.4.2-1

$d\{Z7(x,y)\}/dy = (8)^{0.5}\ 9xy$. 5.4.2-2

So the tilt contribution for square, piston-only micromirrors divided by the RSS aberration for Z7 is

$RSS\ Ratio_{tilt}(Z7) = 68/3\ \eta^2 \approx 18/N$ 5.4.2-3

And the total RSS WFE for an array of square piston-only micromirrors is then

$RSS\ Ratio_{piston}(Z7) \approx RSS\ Ratio_{tilt}(Z7) + RSS\ Ratio_{p\text{-}t\text{-}t}(Z7)$. 5.4.2-4

And the ratio of RMS wavefront errors before and after correction by a piston-only, square array of micromirrors is

$RMSRatio_{piston}(Z7) \approx [\ 18/N + 15/N^2\ ]^{0.5}$. 5.4.2-5

5.4.3 Summary of Zernike error reduction for all micromirror configurations

The low order Zernike terms are listed in Table I. The radius is given by $r^2 \equiv x^2 + y^2$. Note that the defocus, coma, and spherical terms are balanced with lower order aberrations to minimize the RSS WFE errors. These aberrations are orthogonal when integrated over an unobscured circular aperture (the system aperture). Also, they are orthonormal in that the RSS of each aberration integrates out to pi (i.e. $\iint [Z7*Z7]\ dxdy = \pi$).

tilt	$Z2 = 2\ x$
defocus	$Z4 = (3)^{0.5}\ [2\ r^2 - 1\ ]$
astigmatism	$Z5 = (6)^{0.5}\ [\ x^2 - y^2\ ]$
astig. @ 45°	$Z6 = (6)^{0.5}\ 2xy$
coma 3rd	$Z7 = (8)^{0.5}\ x(3r^2 - 2)$
spherical 3rd	$Z9 = (5)^{0.5}\ [\ 6r^4 - 6r^2 + 1\ ]$
spherical 5th	$Z16 = (7)^{0.5}\ [\ 20r^6 - 30\ r^4 + 12\ r^2 - 1\ ]$

Table I: Lower Order Zernike terms

The RMS wavefront errors for the Zernike aberrations listed above can be largely corrected by a sufficiently large array of micromirrors that forms an optimized conjugate phase profile. In Table II, expressions are given for the reduction in RMS WFE for the Zernike aberrations using several different types of micromirror arrays. Included are square arrays of square micromirrors with piston/tip/tilt corrections (sq. p-t-t), hexagonal piston/tip/tilt, (hex p-t-t), piston motion (sq. piston-only), and hexagonal arrays with piston motion (hex piston-only). Note: All of these results were computed in essentially the same way as was done in the example presented in section 5.4.2.

Zernike term		sq. p-t-t	hex p-t-t	sq. piston-only	hex piston-only
Z2	tilt	0	0	$[1.05/N]^{0.5}$	$N^{-0.5}$
Z4	defocus	1.12/N	1/N	$[1.18/N+1.25/N^2]^{0.5}$	$[1.12/N+1/N^2]^{0.5}$
Z5	astigmatism	0.92/N	1/N	$[0.26/N+0.84/N^2]^{0.5}$	$[0.25/N+1/N^2]^{0.5}$
Z6	astig. @ 45°	1.45/N	1/N	$[0.26/N+2.1/N^2]^{0.5}$	$[0.25/N+1/N^2]^{0.5}$
Z7	coma	3.9/N	3.5/N	$[18/N+15/N^2]^{0.5}$	$[14/N+12/N^2]^{0.5}$
Z9	3rd spherical	10.8/N	9.3/N	$[31/N+117/N^2]^{0.5}$	$[30/N+87/N^2]^{0.5}$
Z16	5th spherical	64/N	54/N	$[276/N+4050/N^2]^{0.5}$	$[264/N+2930/N^2]^{0.5}$

Table II: Normalized RMS Reduction of Selected Zernike Aberrations by Micromirror Arrays

The variable "N" is the number of micromirrors in a circular aperture defined by the beam. Note that for small values of N, neither a square nor a hexagonal array will enclose the circular aperture very efficiently. Therefore, the expressions in the following table should be considered as a rough approximation unless N is fairly large (>100). However, for large arrays with hundreds of micromirrors, this data is quite useful for comparing the four different micromirror architectures

5.5 Discussion of Results

Figure 1 shows the residual RMS WFE versus number of micromirrors in the array for hexagonal arrays of micromirrors correcting defocus and third- and fifth-order spherical aberration. Figure 1 shows that an array of about 1000 piston-only micromirrors can correct

defocus (Z4)—reducing the RMS WFE to about 3% of its initial value. From Table II, one can see that astigmatism and tilt can be corrected to about the same degree as defocus. Therefore, an array of about a thousand piston-only micromirrors might be quite sufficient to correct optical systems with a few waves of these lower-order aberrations. By contrast, third-order spherical (Z9) can only be reduced to 8% of its initial value by an array containing 1000 piston mirrors, and it would probably take well over 10,000 micromirrors to reduce fifth-order spherical aberration (Z16) significantly. So it is suggested that arrays of piston-only micromirrors only be used to correct systems with only astigmatism, tilt, and defocus.

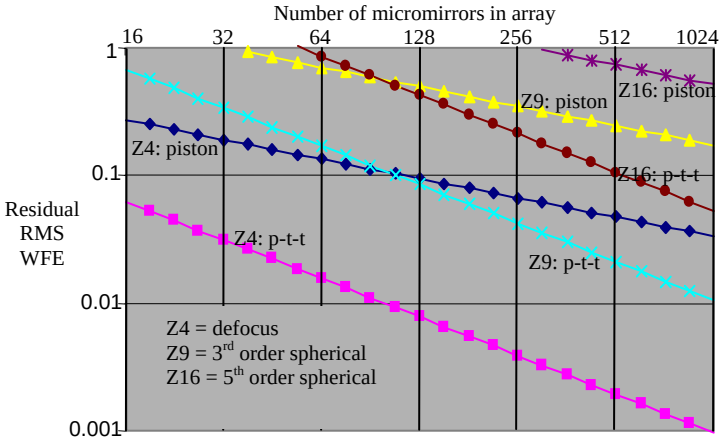

Figure 17. Residual RMS Aberrations After WFE Correction (normalized by the RMS aberration). The Zernike aberrations Z4, Z9 & Z16 are defocus and 3rd and 5th order spherical aberration. The subscripts "$_{piston}$" and "$_{p\text{-}t\text{-}t}$" refer to arrays of piston-only and piston-tip-tilt micromirrors.

As seen in Figure 1, correction of the higher-order aberrations demands the use of piston/tip/tilt micromirror arrays. Even then, it takes an array of 1000 p-t-t micromirrors to reduce the RMS WFE of Z9 by 100X. Remember too that each micromirror has to have three actuators and the wavefront diagnostic must be able to measure the mirror tilts along with the piston motion. The good news is that a 1000-mirror array can reduce the RMS wavefront error of defocus a thousand-fold, third order aberrations by at least a factor of a hundred, and fifth-order aberrations by a factor of at least twenty.

Table II should help the designer choose between a square and a hexagonal array geometry. For piston-only micromirrors, there is almost no difference (≈2.5%) in wavefront improvement between the two geometries. Hence, one should probably choose the square format because it is easier to enclose the aperture with a modest number of square micromirrors than with hexagonal micromirrors.

With piston/tip/tilt mirrors, the hexagonal geometry has significantly better performance over the square geometry. This can be seen in Table II. Note that there is a fairly large difference between the coefficients for the 45° astigmatism term and a significant one for simple defocus.

Arrays of piston-only micromirrors are useful for correcting low-order aberrations including tilt, defocus, and third-order astigmatism, where an array of N = 3000 micromirrors can reduce the RMS wavefront error ~50X. Put in a mathematical form, piston-only micromirrors can reduce

the RMS WFE resulting from defocus and astigmatism by ~$1/N^{0.5}$ for the N > 20. Third-order spherical can be reduced by roughly $5.5/N^{0.5}$.

Higher order aberrations can be far better corrected by piston/tip/tilt micromirrors. For example, 1000 micromirrors can reduce defocus and astigmatism a thousandfold, third-order spherical and coma one-hundredfold, and fifth-order spherical (and most other 5^{th} and 7^{th} order aberrations) ~20X. More formally, the reduction of the RMS WFE for focus and/or astigmatism is approximately proportional to 1/N for an array of "N" tip/tilt/piston micromirrors for N>30. Arrays of tip/tilt/piston mirrors can reduce the RMS WFE of third-order spherical by ~10/N.

Very large hexagonal micromirror arrays (N > 1000) are slightly better at reducing the RMS WFE than are square arrays of the same size. However, with smaller arrays, the array fill factor may become more important.

This page intentionally left blank

6. Summary and Conclusions

This project was based on the premise that there are situations in which having a single imaging system that could have a wide field-of-view (FOV) for surveillance and situational awareness yet quickly and nonmechanically zoom in on an area of interest with higher resolution could be very beneficial. The main limitation to the concept is the relatively small dynamic range of currently available active optically elements. Thus, the most common implementation of nonmechanical zoom is likely for space-based or near space imaging. In these cases, the size of the imaging system can be fairly large which lends itself to the larger optical paths that are required for nonmechanical zoom.

It was hypothesized that we could obtain diffraction-limited, optical zoom by simply changing the voltages that were applied to either a micromachined deformable membrane mirror (MMDM) or a liquid crystal (LC) lens. In fact, we were able to obtain near diffraction-limited results with a reflective optical system using two MMDMs and 3 static, spherical mirrors. Given sufficient time, we are quite certain that diffraction-limited performance is achievable.

While MMDMs were useful for a proof-of-principal demonstration, robustness issues make them a poor choice for fieldable systems. MEMS segmented mirrors can operate in a similar fashion. In addition to being more robust, MEMS mirrors are not electrostatically driven, which means that they do not necessarily impart defocus when they are actuated, as do MMDMs. This increases their functionality for the active optical zoom concept. As part of this effort, we performed a thorough analysis comparing piston-only, segmented MEMS mirrors and piston-tip-tilt mirrors, which showed that piston-tip-tilt can significantly improve the performance of these devices. Segmented, piston-tip-tilt mirrors should provide a robust mechanism for future adaptive optical zoom development.

The LC lenses that were available, both commercially and prototype devices, were not capable of diffraction limited performance. However, the new prototype devices from Holochip, Inc. are close, and we did demonstrate zoom capability using both of these lenses, showing that the concept is viable.

Finally, we also developed a concept for increasing the wavelength bandwidth of an imaging system by integrating a variable focal length LC lens with a nonmechanical spectral filter. Although not directly related to active optical zoom, this idea was spawned as part of this project and may turn out to be extremely useful for some applications. Because axial chromatic aberrations can be eliminated by simply adding defocus, a single optical system could be used to image a wide range (i.e. 400-1700 nm) by simply looking at a single wavelength at any given instant.

This page intentionally left blank

7. References

1. See for example, M. Laikin, *Lens Design, Second Edition*, pp. 301-365, Marcel Dekker, Inc., New York (1995) or R.R. Shannon, *The art and science of optical design*, pp. 533-553, Cambridge University Press, New York (1997).

2. D.V. Wick and T. Martinez, "Adaptive optical zoom," *Opt. Eng.*, **43**, 8-9 (2004).

3. T. Martinez, D.V. Wick, D.M. Payne, J.T. Baker, and S.R. Restaino, "Non-mechanical zoom system," *Proceedings of the SPIE*, **5234**, 375-378 (2003).

4. E.C. Tam, "Smart electro-optical zoom lens," *Opt. Lett.* **17**, 369-371 (1992).

5. A. F. Naumov, G. Love, M. Y. Loktev, and F. L. Vladimirov, "Control optimization of spherical modal liquid crystal lenses ," *Opt. Express* **4**(9)**,** 344-352 (1999).

6. V. Laude, "Twisted-nematic liquid-crystal pixilated lens," *Opt. Comm*. **153**, 134-152 (1998).

7. Y. Takaki and H. Ohzu, " Liquid-crystal active lens: a reconfigurable lens employing a phase modulator," *Opt. Comm*. **126**, 123-134 (1996).

8. R.K. Tyson, *Principles of Adaptive Optics, Second Edition*, Academic Press, San Diego (1998).

9. D.V. Wick, T. Martinez, S.R. Restaino, and B.R. Stone, "Foveated imaging demonstration," *Opt. Express*, **10**, 60-65 (2002).

10. G. D. Love, "Wave-front correction and production of Zernike modes with a liquid-crystal spatial light modulator," *Appl. Opt*. **36**, 1517-1524 (1997).

11. D. M. Pepper, C. J. Gaeta, and P. V. Mitchell, "Real-Time Holography, Innovative Adaptive Optics, and Compensated Optical Processors Using Spatial Light Modulators," Chap. 14 in *Spatial Light Modulator Technology - Materials, Devices, and Applications*, U. Efron, ed., Marcel Dekker, Inc., New York (1995).

12. S. Kuiper and B. Hendriks, "Wet & Wild," *oe magazine*, **5**(1), 20-23 (January 2005).

13. For a detailed explanation of Fresnel zone plates see, for example, E. Hecht, *Optics*, pp. 445-447, Addison-Wesley Publishing Company, Inc., Reading, Massachusetts (1987).

14. D.V. Wick, D.M. Payne, T. Martinez, and S.R. Restaino, "Large dynamic range wavefront control of micromachined deformable membrane mirrors," *to be published in SPIE Proceedings,*, Paper # 5798-26, (Spaceborne Sensors II, Defense and Security Symposium, Orlando, FL 2004).

15. G.V. Vdovin, S. Middelhoek, P. M. Sarro, "Technology and applications of micromachined silicon adaptive mirrors," *Opt. Eng.* **36**, 1382-1390 (1997).

16. See M. Ye, B. Wang, and S. Sato, "Liquid-crystal lens with a focal length that is variable in a wide range," *Appl. Opt.* **43**, 6407-6412 (2004) and references contained therein.

17. A.F. Naumov, M. Yu. Loktev, I.R. Guralnik, and G. Vdovin, "Liquid-crystal adaptive lenses with modal control," *Opt. Lett.* **23**, 992-994 (1998).

18. M.T.Gruenisen, "Wavelength Agile Telescope with Diffractive Wavefront Control and Acousto-Optical Spectral Filter", *Proc. of SPIE*, **5553**,182-188 (2004).

19. M.G. Robinson, J. Chen, and G.D. Sharp, *Polarization Engineering for LCD Projection*, Ch. 6. (Wiley and Sons, Ltd., West Sussex, 2005).

20. G.D. Sharp and J.R. Birge, "Retarder stack technology for color manipulation", *SID Symposium*, **30**, 1072-1075 (1999).

Distribution

1	MS1188	David Wick
1	0972	C. Andy Boye
1	1188	Brett Bagwell
1	0603	William Sweatt
1	1005	Russell D. Skocypec
1	1005	Ray Shaum
1	1010	Charles Duus
1	9018	Central Technical Files, 8945-1
2	0899	Technical Library, 4536
1	0123	LDRD Office-Donna Chavez